Ultrafast Myocardial Principal Strain Ultrasound Elastography During Stress Tests: In Vitro Validation and In Vivo Feasibility

Diya Wang, Boris Chayer, François Destrempes, Jonathan Porée, *Member, IEEE*, Marie-Hélène Roy Cardinal, François Tournoux, and Guy Cloutier, *Senior Member, IEEE*

***Abstract*— Objective myocardial contractility assessment during stress tests aims to improve the diagnosis of myocardial ischemia. Tissue Doppler imaging (TDI) or optical flow (OF) speckle tracking echocardiography (STE) has been used to quantify myocardial contractility at rest. However, this is more challenging during stress tests due to image decorrelation at high heart rates. Moreover, stress tests imply a high frame rate which leads to a limited lateral field of view. Therefore, a large lateral field-of-view robust ultrafast myocardial regularized OF-TDI principal strain estimator has been developed for high-frame-rate echocardiography of coherently compounded transmitted diverging waves. The feasibility and accuracy of the proposed estimator were validated in vitro (using sonomicrometry as the gold standard) and in vivo stress experiments. Compared with OF strain imaging, the proposed estimator improved the accuracy of principal major and minor strains during stress tests, with an average contrast-to-noise ratio improvement of 4.4 ± 2.7 dB (p-value < 0.01). Moreover, there was a significant correlation and a very close agreement between the proposed estimator and sonomicrometry for tested heart rates between 60 and 180 beats per minute (bpm). The averages ± standard deviations (STD) of R^2 and biases ± STD between them were 0.96 ± 0.04 (p-value < 0.01) and 0.01 ± 0.03% in the axial direction, respectively; and 0.94 ± 0.02 (p-value < 0.01) and 0.04 ± 0.06% in the lateral direction, respectively. These results suggest that the proposed estimator could be useful clinically to provide an accurate and quantitative 2-D large lateral field-of-view myocardial strain assessment at high heart rates during stress echocardiography.**

***Index Terms*— Myocardial elastography, optical flow (OF), principal strain, stress test, tissue Doppler, ultrafast ultrasound imaging.**

Manuscript received 26 August 2022; accepted 17 October 2022. Date of publication 21 October 2022; date of current version 28 November 2022. This work was supported in part by the Collaborative Health Research Program of the Natural Sciences and Engineering Research Council of Canada under Grant CHRP-462240-2014, in part by the Canadian Institutes of Health Research under Grant CPG-134748, and in part by a team grant of the Fonds Québécois de Recherche sur la Nature et les Technologies under Grant FQRNT-PR-189822. *(Corresponding author: Guy Cloutier.)*

This work involved human subjects or animals in its research. Approval of all ethical and experimental procedures and protocols was granted by the institutional review board on ethics of the University of Montreal Hospital Research Center under IRB No. #2019-8002.

Diya Wang was with the Laboratory of Biorheology and Medical Ultrasonics, Research Center, University of Montreal Hospital, Montreal, QC H2X 0A9, Canada. He is now with the Key Laboratory of Biomedical Information Engineering of the Ministry of Education, School of Life Science and Technology, Xi'an Jiaotong University, Xi'an 710049, China.

Boris Chayer, François Destrempes, and Marie-Hélène Roy Cardinal are with the Laboratory of Biorheology and Medical Ultrasonics, Research Center, University of Montreal Hospital, Montreal, QC H2X 0A9, Canada.

Jonathan Porée was with the Laboratory of Biorheology and Medical Ultrasonics, Research Center, University of Montreal Hospital, Montreal, QC H2X 0A9, Canada. He is now with the École Polytechnique of Montreal, Montreal, QC H3T 1J4, Canada.

François Tournoux is with the Laboratory of Biorheology and Medical Ultrasonics, Research Center, University of Montreal Hospital, Montreal, QC H2X 0A9, Canada, and also with the Department of Cardiology, Echocardiography Laboratory, University of Montreal Hospital, Montreal, QC H2X 0A9, Canada (e-mail: francois.tournoux@umontreal.ca).

Guy Cloutier is with the Laboratory of Biorheology and Medical Ultrasonics, Research Center, University of Montreal Hospital, Montreal, QC H2X 0A9, Canada, and also with the Department of Radiology, Radio-Oncology and Nuclear Medicine, and Institute of Biomedical Engineering, University of Montreal, Montreal, QC H3C 3J7, Canada (e-mail: guy.cloutier@umontreal.ca).

Digital Object Identifier 10.1109/TUFFC.2022.3216447

I. Introduction

ASSESMENT of myocardial contractility during a stress test is of high clinical value for the diagnosis and evaluation of cardiovascular diseases, especially coronary disease and heart failure [1], [2], [3]. Given its noninvasiveness, portability, and real-time advantages, stress echocardiography is one of the most used techniques to triage patients with suspected cardiovascular diseases when wall motion and/or left ventricular function are normal at rest [1]. Stress echocardiography uses either a pharmacological agent or exercise to reproduce the patient's symptoms. Interpretation of this test is based on a subjective and operator-dependent assessment of wall motion abnormalities [4], as well as myocardial shortening and thickening reflecting the mechanics of the heart [5], [6]. Therefore, 2-D longitudinal, circumferential, and radial strains and strain rate imaging techniques based on tissue Doppler imaging (TDI) [7], [8], [9] and speckle tracking echocardiography (STE) [9], [10], [11] have been developed to objectively quantify myocardial motion and deformation during stress tests [12], [13].

However, current 2-D myocardial strain imaging techniques based on TDI or STE have a few limitations. TDI can track large motions but measured displacements are precise only along the beam direction due to its inherent angle dependency [9], [14]. Although STE is angle-independent and can recover

the 2-D myocardial strain field, tracking methods in STE are sensitive to B-mode speckle intensity variation [15]. STE also requires high contrast and high resolution to ensure accurate tracking of speckle patterns, especially under small motion conditions [16], [17]. Considering that the performance of STE to track small displacements is better than TDI, two myocardial motion estimation models combining TDI with STE have been proposed [15], [18]. To further improve tracking of small myocardial motions, radio-frequency data processing instead of B-mode speckle tracking has also been investigated [16], [17], [19], [20].

Current myocardial strain imaging methods are limited by a tradeoff between spatial and temporal resolutions, and by the lateral field-of-view, especially in the clinical context of stress echocardiography [21]. The typical frame rate (∼60 Hz) of conventional echocardiography is insufficient to warrant accurate strain estimation at high heart rates, where displacements and deformations are emphasized compared with the normal resting condition [22]. Low frame rates and/or high heart rates result in large displacements between consecutive frames and image decorrelation [22], [23], [24], [25], [26], [27]. Over the past few years, ultrafast transthoracic echocardiography and several other techniques have been able to achieve high frame rates (250–12 000 Hz) [27], [28], [29]. Mismatches between multiline acquisitions [30], crosstalk artifacts in multiline transmissions [31], [32], respiratory or inconsistent heartbeat artifacts in electrocardiogram-gated acquisitions [33], and the small lateral field-of-view in compounded plane wave transmissions [34] favored the development of ultrafast compounded diverging wave echocardiography (UCDWE) [27], [28]. UCDWE has been used to estimate myocardial strain with a large lateral field-of-view at rest conditions [17], [24] and under in vitro stress tests in our preliminary study [35]. Sidelobe artifacts with large tilted angle transmissions and undesired phase delays between transmissions, induced by the myocardial motion in UCDWE, have been effectively overcome by using a triangle transmission sequence and coherent compounding with Doppler-based motion compensation at rest conditions [36].

The main challenges linked to stress test conditions are large motions between acquired image frames and the associated image decorrelation. This study aimed to propose a robust UCDWE-based ultrafast myocardial elastography method to overcome the above challenges during stress tests. The following innovations were implemented in this study to optimize myocardial strain imaging under stress test conditions.

1) As suggested in [36], tilting angles of diverging wave transmission were coded as a triangle sequence and motion compensation was considered to reduce sidelobe artifacts in coherent compounding to lessen the impact of decorrelation between frames.
2) As suggested in [15] and [18], the advantages of the TDI component for large motions and the optical flow (OF) component for small deformations [37] were considered, and thus the OF-TDI model was used to balance myocardial motion estimations ranging between large and small deformations during the stress test in systole and diastole, respectively.
3) The time-ensemble strategy proposed in the context of compounded plane wave carotid artery elastography [38], [39] was integrated into the OF-TDI model [15], [18] to build a quadratic temporal–spatial OF-TDI cost function to lessen the influence of out-of-plane motions and to improve the robustness of myocardial displacements estimation.
4) As suggested by others for cardiac [40] and vascular [39], [41] applications, principal strain analysis was combined with a 2-D least-squares strain model and weighted by a Gaussian matrix for myocardial strain estimates to overcome its coordinate system dependency and to improve its accuracy and robustness.

In the context of stress echocardiography tests, a UCDWE-based 2-D least-squares time-ensemble regularized OF-TDI principal strain estimator (OF-TDI$^{\mathrm{TER}}$, where TER signifies time-ensemble regularized) was thus proposed to address the above main challenges and reconstruct myocardial strain fields with high accuracy and robustness. The feasibility of the UCDWE-based OF-TDI$^{\mathrm{TER}}$ principal strain estimator was tested with in vitro and in vivo experiments, and the accuracy was validated by using sonomicrometry at heart rates between 60 and 180 beats per minute (bpm).

II. Methods

Fig. 1 indicates the schematic of myocardial elastography during stress tests using the UCDWE-based OF-TDI$^{\mathrm{TER}}$ principal strain estimator. The proposed estimator has three steps: 1) the UCDWE for stress tests; 2) the quadratic OF-TDI$^{\mathrm{TER}}$ model; and 3) the principal strain estimator.

A. UCDWE for Stress Tests

To reduce artifacts induced by phase delays and sidelobes during stress tests, a triangle diverging wave sequence with M tilted angles at an angular tilt of α and a width of β was transmitted [Fig. 1(a)], which had alternate ascending and descending subsequences as in [36]. The corresponding ascending echoes ($\Re_{2n-1}$, odd) and descending echoes ($\Re_{2n}$, even) were collected from these subsequences. Then, Doppler shift (ϕ) of the fth frame between $\Re_{2n-1}$ and $\Re_{2n}$ was estimated as in the following equation in polar coordinates:

$$\phi_f(r,\theta) = \frac{1}{2}\angle\{\Re_{2n-1}(r,\theta), \Re_{2n}(r,\theta)\} \tag{1}$$

where $f = 2n-1$ is the frame number and n is the transmission number of the triangle diverging wave sequence. To prevent a high Nyquist limit during stress tests, the TDI displacement data ($\mathbb{D}_f$) of the fth frame was estimated before the coherent compounding:

$$\mathbb{D}_f = \phi_f \frac{c \cdot \mathrm{PRF}}{4\pi \cdot f_0 \cdot \mathrm{FR}} \tag{2}$$

where c, PRF, f_0, and FR are the sound speed, the pulse repetition frequency of the triangle diverging wave sequence, the center frequency of the emitted pulse, and the frame rate, respectively. See Table I for a description of the parameters considered in this study.

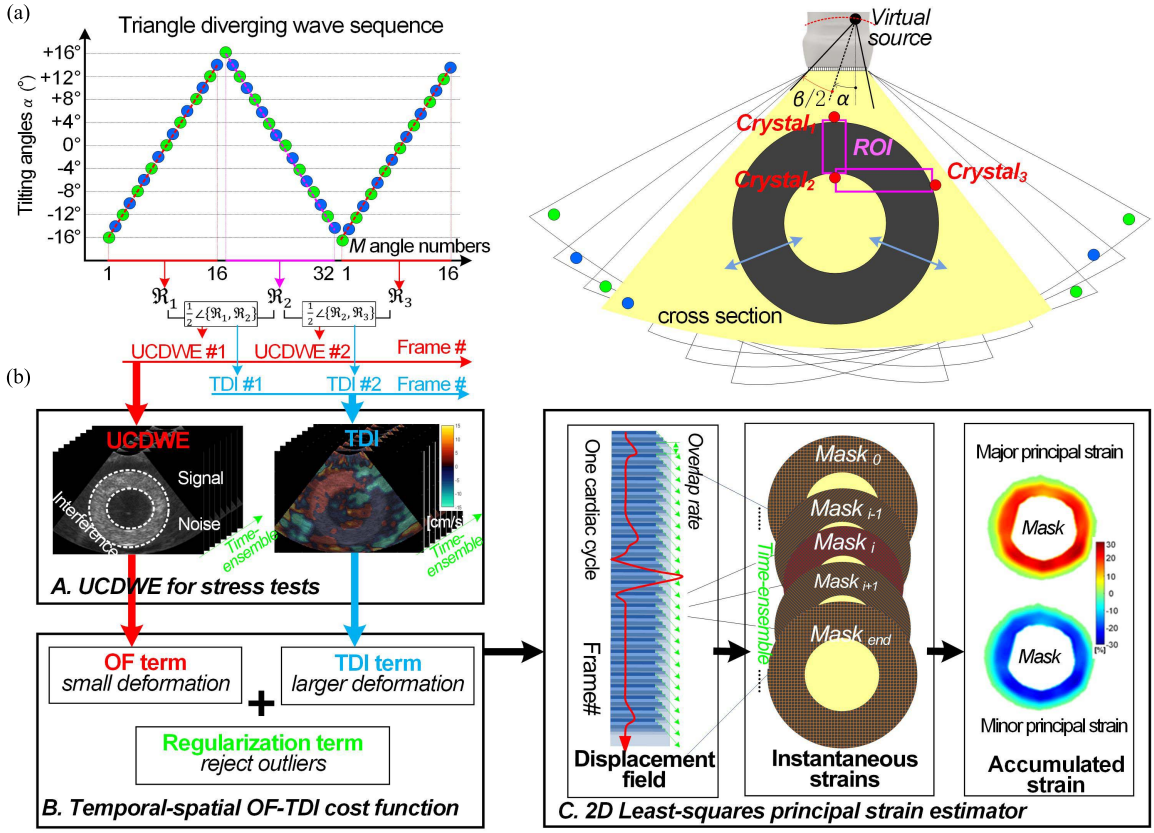

Fig. 1. Schematic of myocardial elastography during stress tests using the ultrafast time-ensemble regularized optical-flow and tissue-Doppler-imaging (OF-TDI^{TER}) principal strain estimator based on UCDWE. (a) UCDWE using a triangle diverging wave sequence in the short-axis view, and (b) diagram of the proposed principal strain estimator using typical in vitro examples during stress tests.

TABLE I
PARAMETER SETTINGS OF THE VERASONICS ULTRASOUND SYSTEM

Phased-array transducer	P4-2, 64 elements
Transmission sequence	Triangle sequences
Pulse repetition frequency (*PRF*)	4000–4500 Hz
Pulse emitted frequency f_0	2.25 MHz
Sampling frequency for raw in-phase/quadrature data	5.0 MHz
Frame rate (*FR*)	500 Hz
Imaging width β	75°–90°
Imaging depth	8–12 cm
Tilting angles α	-16°–+16°
Angle number M	36
Pulse number at each angle	2
Transmitted voltage	16 V
Adjustment parameter p	0.1–0.9
Regularization parameter δ	1/2.5–1/0.25 cm^{-1}
Ispta	27.3 mW/cm^2
Isppa	5.7 W/cm^2
MI	0.4
Probe surface temperature	Room temperature

The function named "mexIQmigLoopCuda.mex64" was used for the delay-and-sum beamforming. The radial and cross spacing of the grid, F-number, and pitch were set to 0.308 mm, 0.29°, 0, and 0.32 mm, respectively. After beamforming, the motion-compensated Doppler shift was considered during coherent compounding, and the UCDWE ($\mathbb{S}_f$) of the fth frame was then reconstructed from the raw in-phase and quadrature (IQ) data. We briefly recall the theory; more details can be found in [36].

$$\mathbb{S}_f(\theta, r) = \sum_{m=1}^{M} \left\langle S_m \left\{ \theta, r + \left(m - \frac{M}{2} \right) \frac{\phi(\theta, r)}{4\pi} \frac{c}{f_0} \right\} e^{im\phi(\theta,r)} \right\rangle \tag{3}$$

where M denotes the number of tilted angles, and S_m is the raw slow-time IQ data at the mth tilted angle. Phases occurring in $\Re_{2n-1}$ and $\Re_{2n}$ subsequences yielded clockwise and counterclockwise rotations of side lobes. The autocorrelation product in (1) removed phase delay artifacts induced by rotations of side lobes in (3).

Thus, both myocardial UCDWE and TDI data can be simultaneously obtained at a wide field of view, a large imaging depth, and a high frame rate.

B. Quadratic Temporal—Spatial OF-TDI Cost Function

$\mathbb{S}_f$ data from (3) were interpolated with a 3:1 factor [17] to improve angular resolution and lateral estimation accuracy, especially at large depths under stress test conditions. The myocardium was semiautomatically segmented using in-house software based on motion estimation and Bayesian modeling [42], and a mask matrix (**M**) of each myocardium

frame was then obtained. To estimate instantaneous myocardial displacements ($\vec{\boldsymbol{u}}$) during stress tests, where decorrelation noise is expected, the OF-TDI model in [15] and [18] was constrained by a time-ensemble strategy and a spatial threshold ξ_c. Moreover, the spatial velocity term was replaced by the temporal–spatial displacement $\vec{\boldsymbol{u}}$. Thus, the OF and TDI terms are, respectively, described by the following equations:

$$\mathbb{Q}_O(\vec{\boldsymbol{u}}_i) = \omega_O \left(\frac{\partial \mathbb{S}}{\partial r} u_r + \frac{\partial \mathbb{S}}{\partial \theta} u_\theta - \frac{-\partial \mathbb{S}}{\partial t} \right)^2 \tag{4}$$

and

$$\mathbb{Q}_D(\vec{\boldsymbol{u}}_i) = \omega_D \left(\frac{\partial \mathbb{D}}{\partial \theta} u_\theta + \frac{\partial \mathbb{D}}{\partial t} - \frac{c \cdot \mathrm{PRF}}{4\pi f_0 \cdot \mathrm{FR}} \phi \right)^2 \tag{5}$$

where $\mathbb{Q}_O$ and $\mathbb{Q}_D$ are the OF and TDI terms, respectively; ω_O and ω_D are weights of $\mathbb{Q}_O$ and $\mathbb{Q}_D$ terms, respectively. $\mathbb{D}$ is the unitary displacement vector in the Doppler direction. The variable $t \in T$ is the time-ensemble dimension, where $T = \{t_1, t_2, \ldots, t_n\}$ is the time-ensemble scale. See Table I for a description of the parameters considered in this study.

Based on (4) and (5), the OF-TDI model in [15] and [18] was then modified by the following quadratic temporal–spatial OF-TDI cost function $\mathbb{Q}$

$$\mathbb{Q}(\vec{\boldsymbol{u}}) = \begin{cases} (1-p) \iint_{m,t} \mathbb{Q}_O(\vec{\boldsymbol{u}}_i) \\ \quad + p \iint_{m,t} \mathbb{Q}_D(\vec{\boldsymbol{u}}_i), & \left|\vec{\boldsymbol{\xi}}\right| < \xi_c/2 \\ (1-p) \iint_{m,t} \mathbb{Q}_O(\vec{\boldsymbol{u}}_i) \\ \quad + p \iint_{m,t} \mathbb{Q}_D(\vec{\boldsymbol{u}}_i) \\ \quad + \delta \iint_{m,t} \mathbb{Q}_R(\vec{\boldsymbol{u}}_i), & \xi_c/2 \le \left|\vec{\boldsymbol{\xi}}\right| \le 2\xi_c \\ 0, & \left|\vec{\boldsymbol{\xi}}\right| > 2\xi_c \end{cases} \tag{6}$$

where $\mathbb{Q}_R$ is the regularization term; $p \in (0, 1)$ is a parameter to balance the relative contribution of $\mathbb{Q}_O$ and $\mathbb{Q}_D$; δ is the regularization parameter of $\mathbb{Q}_R$; and $m \in \mathbf{M}$ is the estimation region.

Inspired by solving issues of the ill-posed cost function of the OF-TDI model proposed in [15] for velocity vector imaging, the $\mathbb{Q}_R$ term based on complex divergence and curl expressions of gradient vectors $\vec{\boldsymbol{u}}$ was simplified in the frequency domain as described by the following equation:

$$\delta \mathbb{Q}_R \xrightarrow{\delta = (1/\xi_c)^4} \left\| \vec{\boldsymbol{\xi}}_i \Big/ \boldsymbol{\xi}_c \right\|^4 \left\| \tilde{\vec{\boldsymbol{u}}}_i \right\|^2 \tag{7}$$

where $\vec{\boldsymbol{\xi}}_i$ are spatial Fourier frequencies of $\vec{\boldsymbol{u}}_i$. δ is defined as a cut-off frequency of $(1/\xi_c)^4$ and ξ_c is known as a spatial threshold to balance the OF-TDI term and the $\mathbb{Q}_R$ term. Thus, (6) was modified. In the case of $\xi_c/2 \le |\vec{\boldsymbol{\xi}}| \le 2\xi_c$, the $\mathbb{Q}$ was constrained by the $\mathbb{Q}_R$ term. In the case of $|\boldsymbol{\xi}| < \xi_c/2$, the $\mathbb{Q}_R$ term was set to zero since the value of the quartet in (7) was very small. In the case of $|\vec{\boldsymbol{\xi}}| > 2\xi_c$, the $\mathbb{Q}_R$ term can reject outliers induced by the rapid myocardial motion at increasing heart rates, which was controlled by the parameter δ.

The two adjustment parameters p and δ of the OF-TDI$^{\mathrm{TER}}$ model were optimized during stress tests. According to ground-truth values from sonomicrometry under stress test conditions, p and δ were varied within two ranges given in Table I, respectively. The parameter optimization and evaluation methods are provided in Section IV-C. Using optimized values of p and δ, the OF-TDI$^{\mathrm{TER}}$ model was then solved as a least-squares problem [15] to minimize the quadratic temporal–spatial cost function (6) iteratively. The weights ω_O and ω_D were updated at each iteration using a bi-square function (H) assigning small weights to pixels with large residuals of $\mathbb{Q}_O$ and $\mathbb{Q}_D$ terms, as in the following equations:

$$\omega_O^{i+1} = \omega_O^0 \cdot \mathrm{H}\left[\mathbb{Q}_O(\vec{\boldsymbol{u}}_i) \big/ \omega_O^i\right] \tag{8}$$

$$\omega_D^{i+1} = \omega_D^0 \cdot \mathrm{H}\left[\mathbb{Q}_D(\vec{\boldsymbol{u}}_i) \big/ \omega_D^i\right] \tag{9}$$

with

$$\omega_O^0 = \omega_D^0 = \frac{c \cdot \mathrm{PRF}}{f_0} \Big/ \left| \sigma_D + \frac{c \cdot \mathrm{PRF}}{2 f_0} - 1 \right| \tag{10}$$

where ω_O^0 and ω_D^0 are the initialization values for ω_O and ω_D during iterations, respectively, and i is the number of iterations. In (10), σ_D is the Doppler standard deviation [15]. The least-squares solution $\vec{\boldsymbol{u}}$ reached convergence after three iterations using updated weighting functions. The smoothed displacement field $\vec{\boldsymbol{u}}$ at the central moment of the time-ensemble scale was finally returned.

C. 2-D Least-Squares Gaussian Weighted OF-TDI^{TER} Principal Strain Estimator

The displacement field $\vec{\boldsymbol{u}}$ in polar coordinates was transformed into Cartesian coordinates, and the instantaneous major and minor strain tensors ($\boldsymbol{\varepsilon}_{\max}(t), \boldsymbol{\varepsilon}_{\min}(t)$) were computed using the following equation [38], [43]:

$$\boldsymbol{\varepsilon}_{\max,\min}(t) = \frac{\boldsymbol{\varepsilon}_{xx,t} + \boldsymbol{\varepsilon}_{zz,t}}{2} \pm \sqrt{\left(\frac{\boldsymbol{\varepsilon}_{xz,t} + \boldsymbol{\varepsilon}_{zx,t}}{2} \right)^2 + \left(\frac{\boldsymbol{\varepsilon}_{xx,t} - \boldsymbol{\varepsilon}_{zz,t}}{2} \right)^2} \tag{11}$$

where $\boldsymbol{\varepsilon}_{xx,t}$ and $\boldsymbol{\varepsilon}_{zz,t}$ are instantaneous myocardial lateral and axial strains, and $\boldsymbol{\varepsilon}_{xz,t}$ and $\boldsymbol{\varepsilon}_{zx,t}$ are corresponding instantaneous shear strains, respectively. These Cartesian strain components were estimated using a 2-D least-squares strain model weighted by a convolutional Gaussian window applied on the 2-D instantaneous displacement field $\vec{\boldsymbol{u}}$, as in the following equations:

$$\boldsymbol{E}_t = (\mathbf{W}\mathbf{G}\mathbf{W}^{\mathrm{T}})^{-1}\mathbf{W}^{\mathrm{T}}\mathbf{G}\mathbf{U}_t \tag{12}$$

with

$$\boldsymbol{E}_t = \begin{bmatrix} \eta_{x,t} & \eta_{z,t} \\ \boldsymbol{\varepsilon}_{xx,t} & \boldsymbol{\varepsilon}_{zx,t} \\ \boldsymbol{\varepsilon}_{xz,t} & \boldsymbol{\varepsilon}_{zz,t} \end{bmatrix} \tag{13}$$

$$\mathbf{W} = \begin{bmatrix} 1 & x_{i-w} & z_{i-w} \\ \vdots & \vdots & \vdots \\ 1 & x_{i+w-1} & z_{i+w-1} \end{bmatrix} \tag{14}$$

$$\mathbf{G} = \begin{bmatrix} g_{x_{i-w}z_{i-w}} & \cdots & g_{x_{i-w}z_{i+w-1}} \\ \vdots & \ddots & \vdots \\ g_{x_{i+w-1}z_{i-w}} & \cdots & g_{x_{i+w-1}z_{i+w-1}} \end{bmatrix} \quad (15)$$

and

$$\mathbf{U}_t = \begin{bmatrix} u_{x_{i-w},t} & u_{z_{i-w},t} \\ \vdots & \vdots \\ u_{x_{i+w-1},t} & u_{z_{i+w-1},t} \end{bmatrix} \quad (16)$$

where $\mathbf{E}_t$ is a matrix of instantaneous Cartesian strain tensors, $\mathbf{W}$ is a location matrix, $\mathbf{G}$ is a Gaussian weighted matrix, and $\mathbf{U}_t$ is an instantaneous displacement matrix constrained by $\mathbf{W}$ in Cartesian coordinates. Components $u_{x,t}$ and $u_{z,t}$ in $\mathbf{U}_t$ are the instantaneous lateral and axial displacements in Cartesian coordinates, which were obtained from the proposed OF-TDI$^{\text{TER}}$ model. In (13), $\eta_{x,t}$ and $\eta_{z,t}$ are constants in lateral and axial directions, respectively. In (14)–(16), i is the central location in the ith $\mathbf{W}$, and w is the half window width of the estimated strain, which is related to ξ_c.

From estimated instantaneous $\boldsymbol{\varepsilon}_{\max}(t)$ and $\boldsymbol{\varepsilon}_{\min}(t)$ within the weighted location window, the accumulated principal major and minor strains ($\boldsymbol{E}_{\max}, \boldsymbol{E}_{\min}$) were constrained by the corresponding time-ensemble mask matrix, and calculated within each cardiac cycle, as in the following iterative summation:

$$\boldsymbol{E}_{\max,\min}(t) = f_t\left[\boldsymbol{E}_{\max,\min}(t-1)\right] + \mathbf{M}(\mathrm{t}) \cdot \boldsymbol{\varepsilon}_{\max,\min}(t) \quad (17)$$

with $\mathrm{T}_1 + 1 \leq t \leq \mathrm{T}_2$, and T_1 and T_2 are the moments of end-diastole and end-systole for accumulated strains in systole, respectively; and the moments of end-systole and end-diastole for accumulated strains in diastole, respectively. Thus, $\boldsymbol{E}_{\max}$ and $\boldsymbol{E}_{\min}$ in systole displayed accumulated results from end-diastole to end-systole, as well as $\boldsymbol{E}_{\max}$ and $\boldsymbol{E}_{\min}$ in diastole reporting accumulated results from end-systole to end-diastole. In (17), f_t is a 2-D linear interpolation function based on the structure location of M at time t. The matrix $\mathbf{M}$ is the segmented full myocardial mask. Thus, the least-squares myocardial principal strain estimator could overcome the limitations of affine strain tensors with centroid and coordinate dependencies [41], [43]. Accumulated principal major strain curves of each cardiac cycle were calculated over time within $\mathbf{M}$ regions from end-diastole to end-systole. The corresponding principal minor strain curves were obtained from end-systole to end-diastole. The strain curves were reset to zero at the beginning of each cycle. Since instantaneous axial strain curves had the best periodicity among all computed strain components, this metric was selected to identify systolic and diastolic phases.

III. Experiments

A. Experimental Setup

Fig. 2 shows the block diagram of the in vitro and in vivo experimental setup. Table I displays the experimental parameter settings. A research ultrasound platform (#Vintage 1-128, Verasonics Inc., Redmond, WA, USA) equipped with a phased-array transducer (ATL P4-2, Philips Ultrasound Inc., Bothell, WA, USA) was used to record raw IQ data of myocardial deformation in a short-axis view. A series of

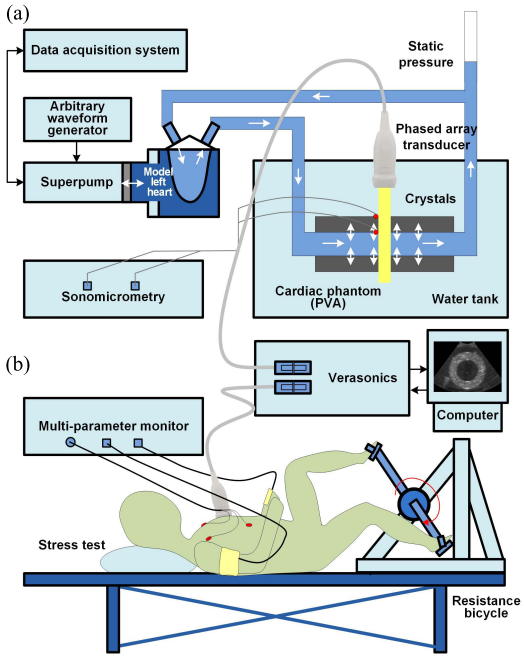

Fig. 2. Block diagram of the (a) in vitro and (b) in vivo experimental setup of myocardial elastography during stress tests.

circular diverging waves were generated by the full array aperture. As shown in Fig. 1(a), those diverging waves were coded and transmitted as a dual triangle sequence with M tilted angles in one angular compounding cycle to perform Doppler-based motion compensation [36].

Before in vitro and in vivo experiments, the pressure of emitted pulses (with parameters reported in Table I) was measured using a 1-mm-diameter needle hydrophone (#SN976, Precision Acoustics, Dorchester, U.K.) in a water tank. Acoustic energy output respected the safety limitations of the Food and Drug Administration standards [44]. All experiments were performed at room temperature, and acquisitions lasted 2 s in vitro and 1.5 s in vivo.

B. In Vitro Cardiac Stress Tests

A dynamic left-ventricular mimicking phantom model with radial thickening and less than 20° of circumferential rotation was used to simulate the left-ventricular deformation in the short-axis direction. The phantom was made with 7% polyvinyl alcohol dissolved in 92% degassed water and mixed with 1% graphite particles [45]. The gel was molded into a homogeneous hollow cylinder and polymerized with two freezing–thawing cycles in a temperature-controlled chamber [46]. Both ends of this left-ventricular mimicking phantom (wall thickness of 15 mm) were then connected to polyvinyl chloride tubing by a pair of loosely attached steel clamps to a pulse duplicator (model #SD2001-1, Vivitro systems Inc., Victoria, BC, Canada), allowing slight rotation of the connecting junctions without leaking. This Vivitro system included an adaptable hydraulic pump (Superpump system, model #10647, Vivitro systems Inc.) and a silicone bag mimicking adult cardiac dimensions suspended in a pressurized container.

Clockwise and counterclockwise rotations of clamps' junctions provided torsion and made the phantom rotate in the circumferential direction. In vitro myocardial strain assessment was tested at artificial heart rates ranging from 60 to 180 bpm, with increments of 20 bpm. Each heartbeat was driven by a sinusoidal wave controlled by a waveform generator (model #33250A, Agilent Inc., Santa Clara, CA, USA). The systolic blood pressure and myocardial deformation were kept within normal ranges at increased heart rates to mimic healthy subject conditions [6], [47], [48]. The in vitro stroke volume at varying heart rates was then adjusted to ensure that accumulated strains within a cardiac cycle remained around 25% at rest and in stress conditions. In vitro experiments were repeated more than three times at each heart rate. For the 2-s data acquisition, six to 18 heart cycles were available for data analysis at heart rates of 60–180 bpm, respectively.

C. Strain Measurements by Sonomicrometry

As shown at three locations marked by red points in Fig. 1(a), piezoelectric crystals (diameter = 2 mm; Sonometric Corporation, London, ON, Canada) were pasted to the internal and external surfaces of the left-ventricular mimicking phantom to accurately detect myocardial deformation in the axial and lateral directions. The sonomicrometry data were considered as axial and lateral ground truths to evaluate the accuracy of myocardial elastography estimated with the proposed ultrafast OF-TDI$^{\text{TER}}$ principal strain estimator. Sonomicrometry data were recorded at a sampling frequency of 200 Hz before UCDWE to avoid band aliasing interferences between the two systems [22]. The axial and lateral sonomicrometry strains were calculated as

$$\varepsilon_a(t) = \Delta D_a(t) \big/ \overline{D_a(t)} \tag{18}$$

$$\varepsilon_l(t) = \Delta D_l(t) \big/ \overline{D_l(t)} \tag{19}$$

where D_a is the intercrystal displacement curve between crystals 1 and 2 and D_l is the intercrystal displacement curve between crystals 2 and 3, which were median filtered with a length of 20 points to reduce noise. ΔD_a and ΔD_l are displacement differences between adjacent temporal samples in the axial and lateral directions, respectively, which matched with the sampling frequency of the proposed ultrafast myocardial elastography method. $\overline{D_a}$ and $\overline{D_l}$ correspond to the mean value of D_a and D_l.

D. In Vivo Cardiac Stress Tests

The in vivo protocol was approved by the institutional review board on ethics of the University of Montreal Hospital Research Center (IRB #2019-8002). As shown in Table II, a healthy male volunteer (#2) and two patients (#1 and #3) with high cardiovascular risk were recruited; all participants signed an informed consent form. Using the same ultrasound system and probe as used in vitro, the probe was first held by a physician, and ultrasound scanning was performed in the parasternal short-axis view at rest condition. As shown in Fig. 2(b), stress tests were performed with a resistance bicycle. During the stress test, the heart rate was recorded with a multiparameter monitoring system (SureSigns VM4, Philips, Andover, MA, USA). The second ultrasound scan in the same parasternal short-axis view was conducted once the heart rate had reached at least 100 bpm. After each data acquisition, the blood pressure was measured using the same multiparameter monitoring system.

TABLE II
IN VIVO CARDIAC STRESS TESTS

No.	Sex	Age	Tests	Repeated acquisitions	Heart rate (bpm)	Blood pressure (mmHg)	
						Diastole	Systole
#01†	Male	72	Rest	2	63.5 ± 0.7	69.5 ± 4.9	141.0 ± 11.3
			Stress	2	104.5 ± 2.1	75.5 ± 2.1	158.5 ± 3.5
#02	Male	57	Rest	3	70.5 ± 3.5	79*	119*
			Stress	3	112.5 ± 3.5	96 ± 15.6	138 ± 15.6
#03†	Male	57	Rest	2	70.6 ± 1.5	74.7 ± 4.0	129.3 ± 5.7
			Stress	2	106.5 ± 3.7	84.7 ± 7.5	148.7 ± 1.5

† subjects with hypertension and high cholesterol, but no heart failure and no coronary disease. *only one value available for this subject (after ultrasound scanning).

IV. DATA ANALYSIS

All postprocessing and data analyses were performed using MATLAB (#2016a, Mathworks Inc., Natick, MA, USA). Results are presented as mean values ± one standard deviation (STD), and p-values < 0.01 were considered statistically significant (t-tests and analyses of variance).

A. Influence of Stress Tests on Ultrafast Echocardiography

With increasing heart rates during the stress test, the effect of signal decorrelation between UCDWE transmissions on image quality was evaluated by the signal-to-noise ratio (SNR) and signal-to-interference ratio (SIR), respectively, using the following equations [39]:

$$\text{SNR} = 10\log\left[\overline{\mathbb{R}}_s / \overline{\mathbb{R}}_n\right] \tag{20}$$

and

$$\text{SIR} = 10\log\left[\overline{\mathbb{R}}_s / \overline{\mathbb{R}}_i\right] \tag{21}$$

where $\overline{\mathbb{R}}_s$ is the average intensity of the myocardial UCDWE; and $\overline{\mathbb{R}}_n$ and $\overline{\mathbb{R}}_i$ are average intensities of noise and sidelobe interferences in regions marked in Fig. 1(b), respectively.

B. Contrast-to-Noise Ratio of Ultrafast Myocardial Elastography

The imaging quality of strain maps $\boldsymbol{E}_{\max,\min}$ estimated with the proposed ultrafast elastography model was quantified by using the instantaneous elastographic contrast-to-noise ratio (CNR_e), as given by the following equation [39]:

$$\text{CNR}_e = 10\log\left[\frac{2\left(\overline{\boldsymbol{E}}_{\max,\min,r_1} - \overline{\boldsymbol{E}}_{\max,\min,r_2}\right)^2}{\sigma\left(\boldsymbol{E}_{\max,\min,r_1}\right)^2 + \sigma\left(\boldsymbol{E}_{\max,\min,r_2}\right)^2}\right] \tag{22}$$

where $\overline{\boldsymbol{E}}_{\max,\min,r_1}$ and $\overline{\boldsymbol{E}}_{\max,\min,r_2}$, and $\sigma(\overline{\boldsymbol{E}}_{\max,\min,r_1})$ and $\sigma(\overline{\boldsymbol{E}}_{\max,\min,r_2})$ are means and STDs of $\boldsymbol{E}_{\max,\min}$ computed along circles of radii $r_1 \in \{R_{\text{inner}}(t) + 3\ R_{\text{inner}}(t) + 5\}$ mm

and $r_2 \in \{R_{\text{outer}}(t) - 5\ R_{\text{outer}}(t) - 3\}$ mm. R_{inner} and R_{outer} are inner and outer radii of the in vitro cardiac phantom, respectively. Above strain maps $\boldsymbol{E}_{\max,\min}$, obtained with the proposed ultrafast myocardial OF-TDI$^{\text{TER}}$ principal strain estimator, should be constant over the circumferential direction due to its cylindrical geometry, which was further compared with principal strain maps estimated by using the OF speckle tracking method when $p = 0$.

C. Accuracy Evaluation and Parameter Optimization of the Proposed Ultrafast Myocardial Elastography Method

The accuracy and parameter optimization of the proposed ultrafast myocardial OF-TDI$^{\text{TER}}$ principal strain estimator were evaluated by computing the agreement between the sonomicrometry and elastography strains by using the correlation coefficients R^2 in axial and lateral directions as in (23) and (24), shown at the bottom of the page, where R^2_{zz} and R^2_{xx} are the correlation coefficients of axial and lateral strains, respectively. N is the length of time series during one cardiac cycle. $\boldsymbol{\varepsilon}_{zz}$ and $\boldsymbol{\varepsilon}_{xx}$ are axial and lateral elastography components averaged within the regions of interest (ROIs) marked by the pink solid-line boxes in Fig. 1(a), respectively. To suppress artifacts from crystals and position shifts during stress tests, these ROIs had a larger size and their central positions were compensated by the central position of $\mathbf{M}$. Parameters $\boldsymbol{\varepsilon}_a$ and $\boldsymbol{\varepsilon}_l$ are axial and lateral sonomicrometry strains, respectively. A Bland–Altman analysis was also performed to illustrate the agreement between sonomicrometry and elastography using the bias and STD between them. Bias is the deviation of mean values between them.

V. Results

A. Ultrafast Echocardiography During Stress Tests

Fig. 1(b) displays examples of in vitro myocardial UCDWE images at a heart rate of 180 bpm in diastole. The influence of signal decorrelation between emissions at increased heart rates during stress tests on UCDWE image reconstructions is illustrated by SNR and SIR curves in Fig. 3(a) and (b), respectively. Compared with measurements at 60 bpm, the mean SNR of UCDWE images decreased by 0.03 dB/10 bpm (residuals: 0.07 dB) during simulated stress tests; the corresponding SIR decreased by 0.14 dB/10 bpm (residuals: 0.25 dB). By contrast, the SIR reduced more than SNR with the increase in heart rate. It suggests that sidelobe interferences had a higher impact on the degradation of UCDWE images at increased heart rates.

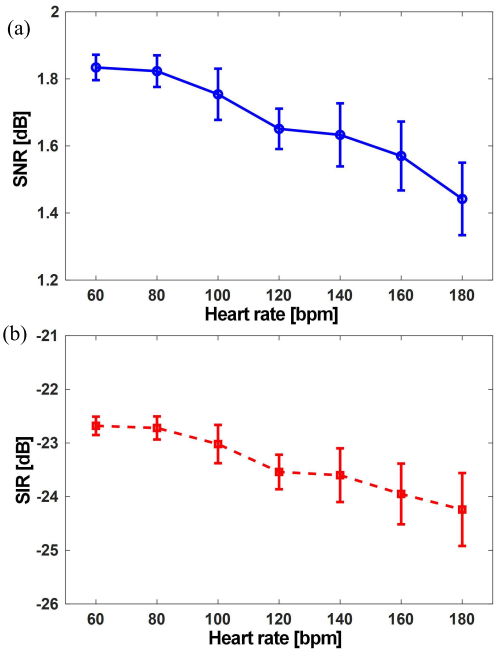

Fig. 3. (a) Signal-to-noise ratio (SNR) and (b) signal-to-interference ratio (SIR) of in vitro myocardial echocardiography during stress tests, at heart rates ranging from 60 to 180 bpm.

B. Accuracy Evaluation and Parameter Optimization According to Sonomicrometry

Cycle durations and amplitudes of estimated instantaneous strain curves correctly matched those of sonomicrometry strain curves. In this study, the sonomicrometry was taken as ground truths to tune parameters p and δ during stress tests and to evaluate the accuracy of the proposed ultrafast OF-TDI$^{\text{TER}}$ principal strain estimator in the axial and lateral directions. Fig. 4 shows corresponding results in the axial direction. With the increase in the parameter δ, the average STD between sonomicrometry and estimated elastography, for different values of p, increased but their average R^2_{zz} tended to decrease at all tested heart rates, especially for smaller p values. In general, the STD was the smallest and R^2_{zz} the highest at all tested heart rates when the parameter δ was 1/0.5 cm^{-1}. Moreover, with the increase in the parameter p from 0.1 to 0.9, the STD decreased and then increased whereas R^2_{zz} slightly decreased for $\delta = 1/0.5$ cm^{-1} at all tested heart rates. When the parameter p was equal to 0.6 for $\delta = 1/0.5$ cm^{-1}, the STD was close to its smallest value at a heart rate of 60 bpm, and the smallest at other heart rates of 120 and 180 bpm; and R^2_{zz} was the highest at the

$$R^2_{zz} = \frac{N\sum_{i=1}^{N}\boldsymbol{\varepsilon}_{zz}(i)\boldsymbol{\varepsilon}_a(i) - \sum_{i=1}^{N}\boldsymbol{\varepsilon}_{zz}(i)\sum_{i=1}^{N}\boldsymbol{\varepsilon}_a(i)}{\sqrt{N\sum_{i=1}^{N}\left[\boldsymbol{\varepsilon}_{zz}(i)\right]^2 - \left[\sum_{i=1}^{N}\boldsymbol{\varepsilon}_{zz}(i)\right]^2}\cdot\sqrt{N\sum_{i=1}^{N}[\boldsymbol{\varepsilon}_a(i)]^2 - \left[\sum_{i=1}^{N}\boldsymbol{\varepsilon}_a(i)\right]^2}} \tag{23}$$

$$R^2_{xx} = \frac{N\sum_{i=1}^{N}\boldsymbol{\varepsilon}_{xx}(i)\boldsymbol{\varepsilon}_l(i) - \sum_{i=1}^{N}\boldsymbol{\varepsilon}_{xx}(i)\sum_{i=1}^{N}\boldsymbol{\varepsilon}_l(i)}{\sqrt{N\sum_{i=1}^{N}[\boldsymbol{\varepsilon}_{xx}(i)]^2 - \left[\sum_{i=1}^{N}\boldsymbol{\varepsilon}_{xx}(i)\right]^2}\cdot\sqrt{N\sum_{i=1}^{N}[\boldsymbol{\varepsilon}_l(i)]^2 - \left[\sum_{i=1}^{N}\boldsymbol{\varepsilon}_l(i)\right]^2}} \tag{24}$$

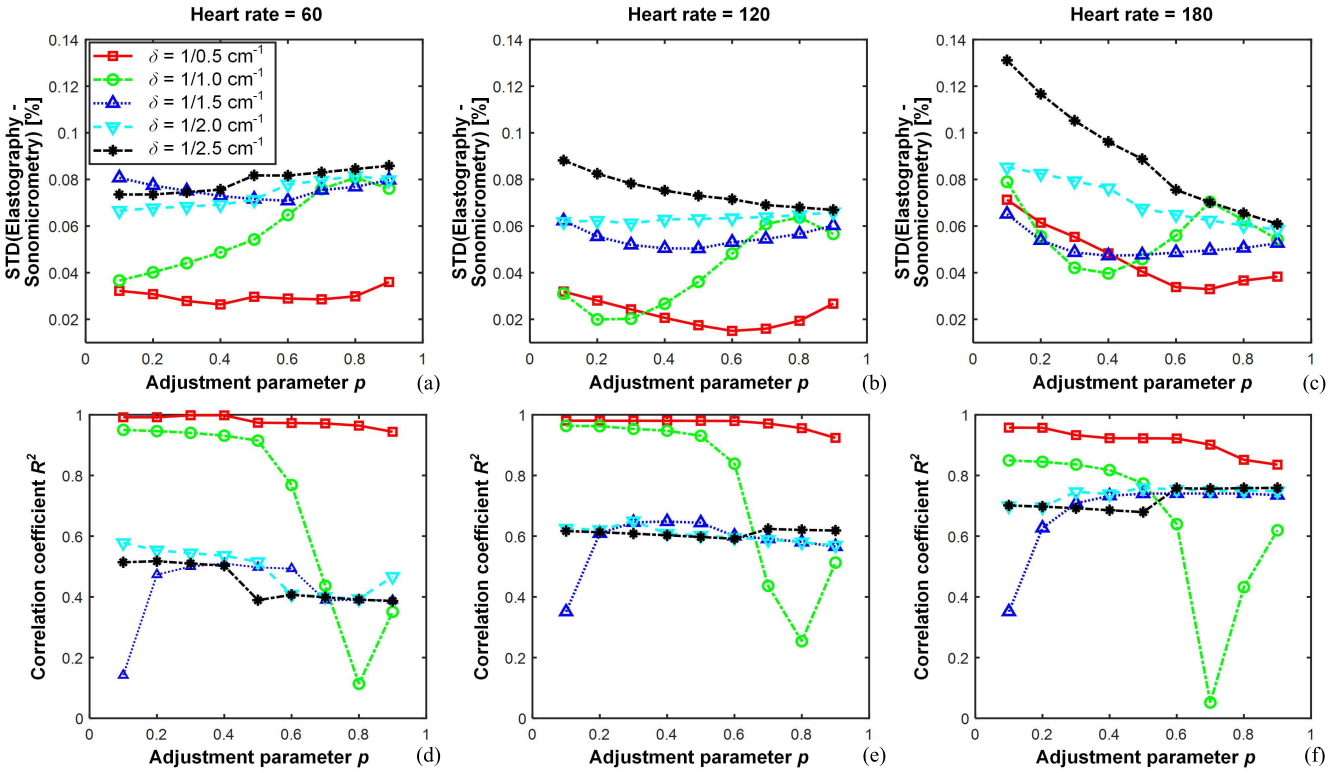

Fig. 4. Accuracy evaluation and parameter optimization of the proposed ultrafast OF-TDI$^{\text{TER}}$ principal strain estimator using ground truths measured with sonomicrometry. Heart rates of 60, 120, and 180 bpm are presented. (a)–(c) Standard deviation (STD) and (d)–(f) correlation coefficient R^2 in Bland–Altman analysis between sonomicrometry and elastography at various adjustment parameter p and regularization parameter δ.

heart rate of 120 bpm and very close to its maximum at heart rates of 60 and 180 bpm. Therefore, the adjustment parameter $p = 0.6$ and the regularization parameter $\delta = 1/0.5$ cm^{-1} were selected for the remaining results to be presented, which was also supported by the results in the lateral direction. Using the above-optimized parameters, the STD, bias, and R^2_{zz} between both strain methods in the axial direction were $0.03 \pm 0.01\%$, $0.01 \pm 0.004\%$, and 0.96 ± 0.04 (p-value < 0.01) during stress tests, respectively. Moreover, the corresponding STD, bias, and R^2_{xx} in the lateral direction were $0.06 \pm 0.02\%$, $0.04 \pm 0.01\%$, and 0.94 ± 0.02 (p-value < 0.01), respectively.

C. In Vitro Myocardial Principal Strain During Stress Tests

Fig. 5 shows in vitro myocardial accumulated principal major and minor strain maps at systole and diastole during stress tests computed with the proposed ultrafast OF-TDI$^{\text{TER}}$ estimator. Fig. 6 displays the corresponding principal major and minor strain maps estimated with the OF speckle tracking method for comparison. Compared to OF-based strain maps, more consistent elastograms were obtained with the proposed OF-TDI$^{\text{TER}}$ principal strain algorithm at increased heart rates. Since a homogeneous left-ventricular mimicking phantom was used and because the pump was adjusted to obtain similar stress conditions between experiments, principal major and minor strain maps were quasi-centrosymmetric (except for relatively lower strains in the anterior wall induced by crystals' artifacts) and had similar deformations at increased heart rates. Observed accumulated principal major and minor strains were around $\pm$ 25%, respectively. Absolute values of accumulated principal major and minor strains in systole showed close-to-zero values near the lumen and maximum values close to the periphery, which are proportional to the radius. Corresponding values in diastole showed maximum values near the lumen and close-to-zero values close to the periphery, which are inversely proportional to the radius during the stress test.

The myocardial principal strain maps estimated with the proposed ultrafast OF-TDI$^{\text{TER}}$ strain estimator and OF speckle tracking method were further evaluated by CNR$_e$ in Fig. 7. ROIs with radii r_1 and r_2 that were used to computer CNR$_e$ are displayed in Figs. 5(a) and 6(a). Compared to results obtained with the OF speckle tracking method, the proposed OF-TDI$^{\text{TER}}$ estimator was not affected by the heart rate. CNR$_e$ of major and minor strain components of the OF speckle tracking method decreased by 8.0 ± 1.5 and 8.7 ± 1.6 dB at the highest heart rate of 180 bpm, respectively. Pooling all tested heartbeats, the mean CNR$_e$ of OF-TDI$^{\text{TER}}$ principal major and minor strains were 4.7 ± 2.6 dB (p-value < 0.01) and 4.1 ± 3.1 dB (p-value < 0.01) larger than the corresponding CNR$_e$ obtained with the OF speckle tracking method, respectively. Fig. 8 shows the averaged accumulated principal major and minor strain curves within the segmented myocardial mask at increasing heart rates during stress tests. Since the reference cardiac phases of those accumulated strain curves were identified by the instantaneous axial strain curves

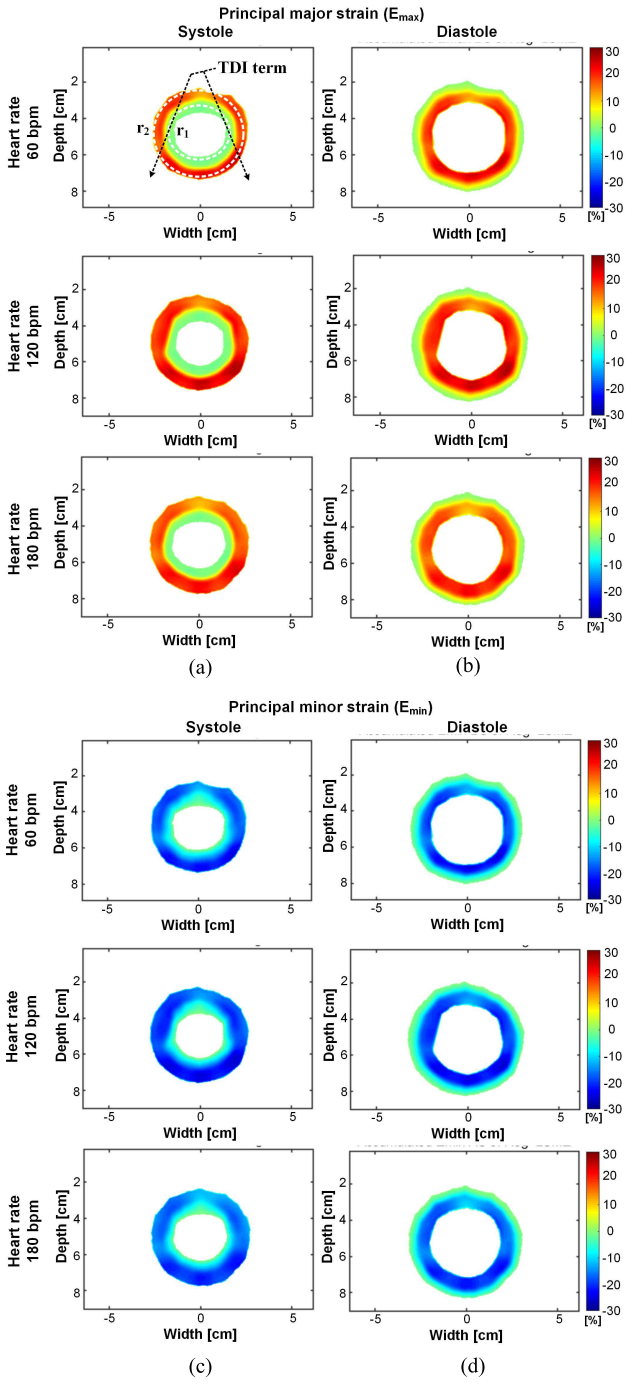

Fig. 5. In vitro myocardial accumulated principal major strain maps in systole (a) and diastole (b) estimated by the proposed ultrafast myocardial OF-TDI^{TER} principal strain estimator during stress tests; corresponding principal minor strain maps in systole (c) and diastole (d).

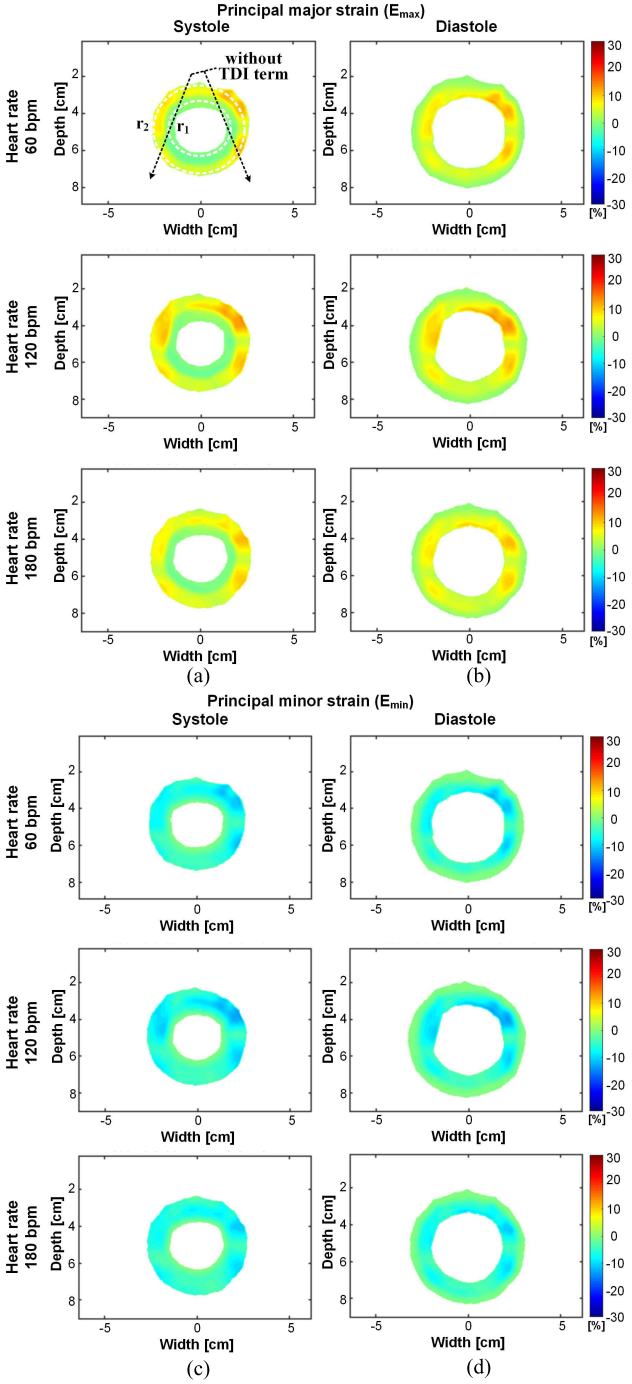

Fig. 6. In vitro myocardial accumulated principal major strain maps in systole (a) and diastole (b) estimated by the OF speckle tracking method during stress tests; corresponding principal minor strain maps in systole (c) and diastole (d).

and were reset to zero at the beginning of each cycle, those strain curves were discontinuous between the end of the last cycle and the beginning of the next cycle.

D. In Vivo Myocardial Principal Strain During Stress Tests

Fig. 9 shows examples of in vivo myocardial accumulated principal major and minor strain maps at systole and diastole before and after stress tests for the OF-TDI^{TER} estimator. The corresponding echocardiography in Fig. 9 indicates the cardiac orientation in the parasternal short-axis view before and after stress tests. Before and after stress tests, absolute values of myocardial principal major and minor strains increased from the lumen to the periphery in systole and reduced from the periphery to the lumen at the same radial positions in diastole. Maximum strains were located on both sides of the left ventricle in this short-axis view. Absolute peak values at specific

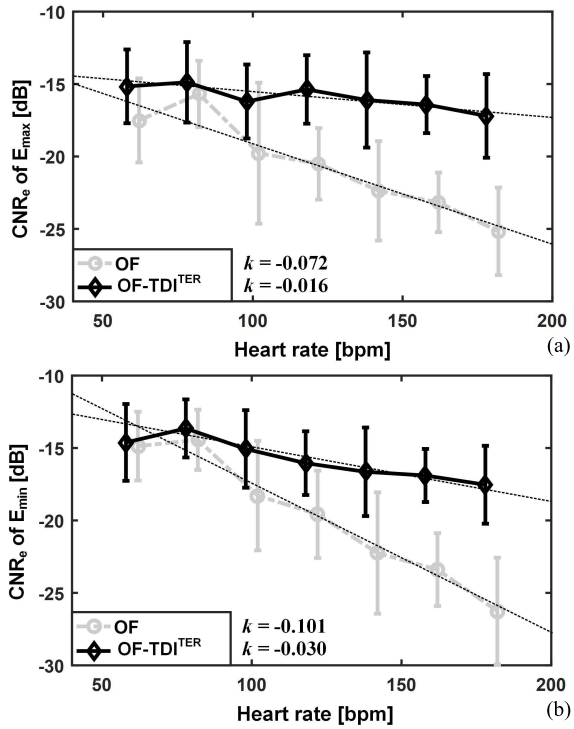

Fig. 7. Myocardial contrast-to-noise ratio (CNR_e) of accumulated principal major (a) and minor (b) strains obtained with the proposed ultrafast OF-TDI^{TER} estimator, and OF speckle tracking method. The parameter k is the fitting coefficient of CNR_e linear regressions.

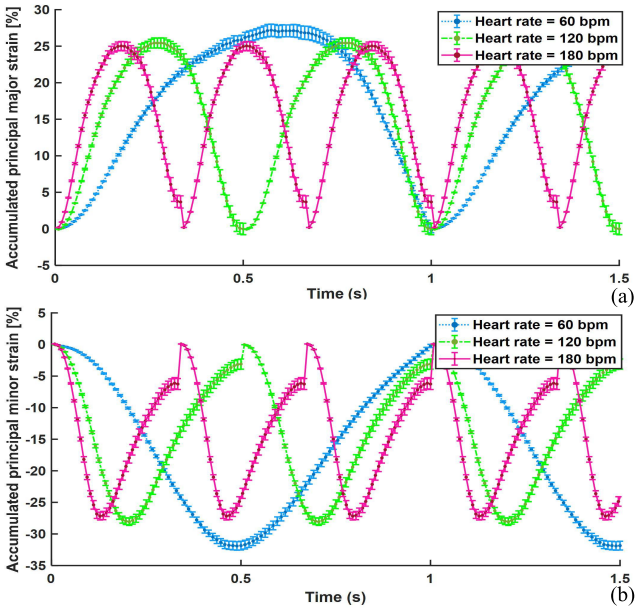

Fig. 8. In vitro myocardial accumulated principal major (a) and minor (b) strain curves at different heart rates using the proposed ultrafast OF-TDI^{TER} estimator. The boxes represent the STD values of accumulated strain maps at each moment.

myocardial locations of principal major and minor strain maps were about 25% at a heart rate of 70 bpm before the stress test, and around 30% at the increased heart rate of 112 bpm after

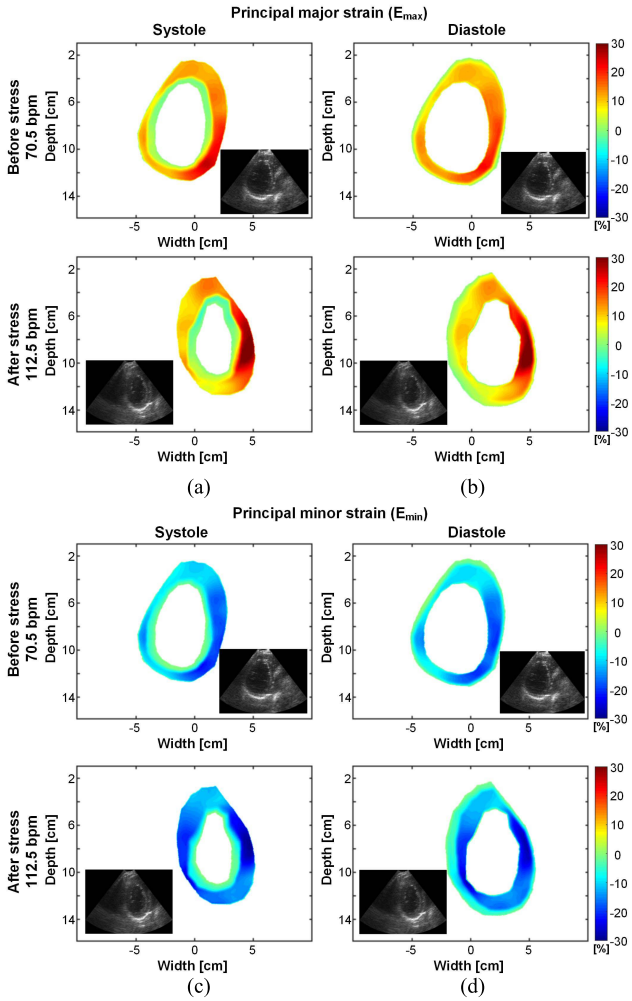

Fig. 9. In vivo myocardial accumulated principal major strain maps in systole (a) and diastole (b) estimated with the proposed ultrafast OF-TDI^{TER} estimator before and after stress tests for patient #3; corresponding principal minor strain maps in systole (c) and diastole (d).

TABLE III
AVERAGED VALUES OF MAXIMUM ACCUMULATED STRAINS FOR IN VIVO CASES*

No.	Tests	Principal major strain (%)		Principal minor strain (%)	
		Diastole	Systole	Diastole	Systole
#01	Rest	16.4 ± 4.3	17.4 ± 3.9	-17.4 ± 3.6	-16.6 ± 2.6
	Stress	21.9 ± 2.6	24.1 ± 2.3	-23.7 ± 6.7	-24.1 ± 5.1
#02	Rest	24.6 ± 2.3	28.2 ± 2.7	-26.9 ± 3.5	-26.6 ± 2.8
	Stress	24.7 ± 2.9	26.7 ± 2.0	-26.8 ± 3.2	-26.1 ± 2.5
#03	Rest	16.7 ± 4.3	17.9 ± 3.6	-17.3 ± 3.7	-16.6 ± 2.7
	Stress	22.1 ± 2.7	24.7 ± 2.9	-23.5 ± 6.5	-25.1 ± 6.7

* The maximum corresponds to the end systole and end diastole of each cardiac cycle.

the stress test. Fig. 10 displays corresponding averaged values within the segmented myocardium of accumulated principal major and minor strain maps for this example. Table III is summarizing the maximum values of accumulated principal major and minor strains, in systole and diastole, averaged over the number of available cardiac cycles and acquisitions for all in vivo cases.

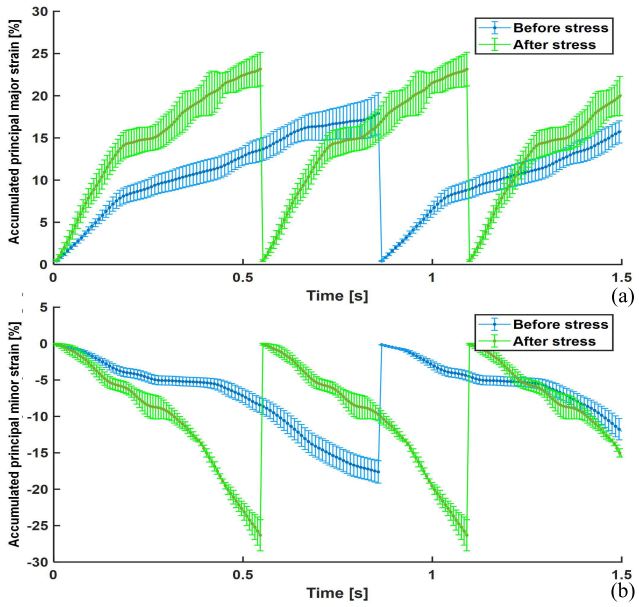

Fig. 10. In vivo myocardial accumulated principal major (a) and minor (b) strain curves before and after stress tests using the proposed ultrafast OF-TDI^{TER} estimator (data for patient #3). The boxes represent the STD values of accumulated strain maps at each moment.

VI. Discussion

A. Tuning Parameters in the OF-TDI^{TER} Principal Strain Estimator

Four parameters had to be optimized with the proposed ultrafast OF-TDI^{TER} principal strain estimator: the two weighting parameters ω_{of} and ω_{tdi}, the adjustment parameter p, and the regularization parameter δ. Values of ω_{of} and ω_{tdi} of OF and TDI terms were automatically iteratively updated according to (5) and (6). The parameter p was used to adjust the relative contribution of OF and TDI terms, and it was selected according to Fig. 4. The parameter δ was selected to balance the OF-TDI and regularization terms, and to reject outliers of $\vec{\boldsymbol{u}}$ at increased heart rates. The parameters p and δ were tuned via the estimation accuracy of the proposed strain estimator using four indices (STD, bias, R^2, and p-values) in agreement and Bland–Altman analyses between sonomicrometry and elastography. Values of $p = 0.6$ and $\delta = 1/0.5$ cm^{-1} provided the highest accuracy of the proposed strain estimator. Additionally, STD and R^2 were more sensitive to the parameter δ than p in Fig. 4. The different sensitivities for p and δ are consistent with results in [18]. On the other hand, Porée et al. [15] averaged the contributions of OF and TDI terms in their OF-TDI model under resting conditions, and then set $p = 0.5$. They considered the upper bound (1.5 cm) of the normal septal thickness of the left ventricular mid-cavity and then fixed $\delta = 1/1.5$ cm^{-1} without other objective evaluations [15]. Tavakoli et al. fixed the weight for the OF term and simplified the tuning process for adjustment and regularization parameters using a relative mean absolute error between the first and subsequent warped images [18]. However, those simplifications could not assure optimal accuracy, had no ground truth for comparison, and could be limitations for stress myocardial elastography studies due to large decorrelation artifacts between strain images. Moreover, the above tuning of parameters would be difficult under in vivo conditions due to the absence of ground truths on in vivo myocardial deformation. Even so, the above tuning and optimization of parameters provided an agreement analysis and accuracy evaluation under both resting and stress test conditions, which supplement the findings of previous studies [15], [18].

B. Comparison With OF Speckle Tracking Elastography

Speckle tracking elastography based on the OF method was compared with the proposed ultrafast OF-TDI^{TER} principal strain estimator. Previous reports demonstrated that the OF method is suitable for estimating small deformations but is sensitive to large instantaneous signal decorrelation [15], [49]. This was also shown on principal major and minor strain maps obtained with the OF method during stress tests in Fig. 6. As shown near the lumen in systole and at the periphery in diastole, the homogeneous and centrosymmetric major and minor strain maps were accurately estimated by the OF method since absolute strain values were within 4% of OF-TDI^{TER} principal strain measures. However, compared with the results in Fig. 5, underestimations were observed with the OF algorithm for absolute strain ranges $\geqq 10\%$. Moreover, compared with the results of the proposed principal strain estimator, averaged CNR$_e$ of principal major and minor strains for the OF method were smaller by 4.4 ± 2.7 dB (p-value < 0.01) during stress tests. These comparisons illustrated that the proposed ultrafast OF-TDI^{TER} principal strain estimator could depict myocardial deformation with a larger range during stress tests. These comparisons supported results reported in [15] and [49] and the corresponding quantification supplemented cardiac studies using the OF-TDI model at rest and stress conditions [15], [18].

C. Contribution of the TDI Term

The TDI method assesses myocardial motion based on the Doppler frequency shift, which is suitable for large tissue displacements [7], [8], [9]. By comparing regions between Doppler beams marked by two black arrows in Figs. 4(a) and 5(a), large deformations could be estimated by the TDI term but the OF term alone provided less accurate results. However, large strains between Doppler beams obtained with the proposed method were not the same as outside Doppler beams. This suggests that the inherent angle dependency of the TDI method [14], [21] could contribute to angular artifacts in strain estimates for motions not aligned with the Doppler ultrasound beam. In this study, the angle-dependent TDI term was balanced by the OF term. Consequently, as seen in strain maps of Fig. 5 within the periphery in systole and near the lumen in diastole, TDI terms described larger myocardial deformations properly, which were centrosymmetric and homogeneous. Moreover, compared with the same strain maps obtained with the OF method in Fig. 6, the TDI term also contributed to eliminating strain artifacts near the periphery in systole and near the lumen in diastole, and it overcame the underestimation of large

myocardial deformations, especially at increasing heart rates (up to 180 bpm). Therefore, the proposed ultrafast OF-TDI^{TER} principal strain estimator integrated both advantages of the affine deformation tracking of the OF method, and the efficacy of TDI to measure larger deformations.

D. Influence of Echo-Decorrelation on Ultrafast Elastography During Stress Tests

Compared with conventional echocardiography at a low frame rate, decorrelation artifacts could be reduced and estimation accuracy of elastography could thus be significantly improved using ultrafast echocardiography [22], [23], [24], [25], [26], [27]. The performance of strain estimators in the context of UCDWE still depends on the contrast and resolution of reconstructed images [17], especially during stress tests. Echo decorrelation induced by sidelobe interferences at large tilted angle emission would deteriorate UCDWE and thus remains a challenge for the evaluation of myocardial contractile function during stress tests. At rest, interferences from phase delays and sidelobes on UCDWE were reduced by using coherent compounding with the TDI motion compensation strategy proposed in [36]. Although UCDWE and corresponding in vitro elastograms were similar at heart rates of 60, 120, and 180 bpm, influences of echo decorrelation on UCDWE and elastograms were still observed after stress tests. These influences were illustrated by decreases in SNR and SIR of UCDWE (Fig. 3), reduced R^2 (Fig. 4), decreased CNR$_e$ of elastograms (Fig. 7), and increased discontinuities of accumulated strain curves (Fig. 8). The decreases in SNR and SIR were slight and only 0.03 dB/10 bpm and 0.14 dB/10 bpm at increasing heart rates, respectively. However, it resulted in a decrease in R^2 of 5%, and in an average CNR$_e$ of principal strain elastograms of 2.5 dB during stress tests. The myocardial elastograms under stress conditions and reconstructed by the proposed strain estimator exhibited a high accuracy in the axial direction (STD $= 0.03 \pm 0.01\%$, $R^2 = 0.96 \pm 0.03$, p-value < 0.01) and in the lateral direction (STD $= 0.06 \pm 0.02\%$, $R^2 = 0.94 \pm 0.02$, p-value < 0.01) during stress tests. Therefore, echo decorrelation and sidelobe interferences had not an obvious impact on strain estimations at increasing heart rates.

E. In Vitro and In Vivo Validations and Limitations

The designed left-ventricular mimicking phantom model had realistic dimension and elasticity in the short-axis view, had physiologically realistic changes in blood pressure and deformation during a cardiac cycle, and stress tests with increased heart rates could also mimic realistic cardiac conditions. The echo decorrelation between frames induced by out-of-plane motion was weakened by the UCDWE method providing a high frame rate, which was further addressed by the time-ensemble estimation strategy of the proposed strain estimator. However, due to limitations of the experimental setup, this heart model could not perfectly simulate the myocardial 3-D torsion and deformation, which could impact the optimization of parameters and should be considered in future works.

Compared with in vitro results, in vivo elastograms displayed some heterogeneities. Because in vivo cases had different pressure distributions, boundary conditions, and a noncentrosymmetric structure in the short-axis view, strain maps had different strain distribution than in vitro results, which may have contributed to emphasizing accumulated strain discontinuities. Compared with absolute values of maximum accumulated strains in patients, the healthy volunteer had larger strain values (Table III). Although the feasibility of the proposed strain estimator could be illustrated by these in vivo validations, the sample size was limited in this study. Therefore, more clinical validations would be required to state the performance and clinical significance of the proposed strain algorithm combined with UCDWE for normal and stress test assessments of patients with cardiac pathologies.

VII. Conclusion

This study proposed a robust ultrafast OF-TDI^{TER} principal strain estimator to assess myocardial contractility during stress tests. Feasibility and accuracy were validated by in vitro and in vivo myocardial stress experiments. The proposed strain estimator overcame lateral field-of-view and frame rate limitations, and artifacts due to sidelobe interferences and image decorrelation during stress tests. The complex, large, and rapid myocardial deformation during stress tests were also accurately imaged by the proposed strain estimator with a close agreement with sonomicrometry.

References

[1] N. Gaibazzi, F. Pigazzani, C. Reverberi, and T. R. Porter, "Rest global longitudinal 2D strain to detect coronary artery disease in patients undergoing stress echocardiography: A comparison with wall-motion and coronary flow reserve responses," *Echo Res. Pract.*, vol. 1, no. 2, pp. 61–70, Nov. 2014.

[2] B. D. Hoit, "Strain and strain rate echocardiography and coronary artery disease," *Circulat., Cardiovascular Imag.*, vol. 4, no. 2, pp. 179–190, Mar. 2011.

[3] M. Vejdani-Jahromi, J. Freedman, M. Nagle, Y.-J. Kim, G. E. Trahey, and P. D. Wolf, "Quantifying myocardial contractility changes using ultrasound-based shear wave elastography," *J. Amer. Soc. Echocardiography*, vol. 30, no. 1, pp. 90–96, Jan. 2017.

[4] V. Uusitalo et al., "Two-dimensional speckle-tracking during dobutamine stress echocardiography in the detection of myocardial ischemia in patients with suspected coronary artery disease," *J. Amer. Soc. Echocardiogr.*, vol. 29, no. 5, pp. 470–479, May 2016.

[5] T. H. Marwick, "Stress echocardiography," in *Echocardiography*. Boston, MA, USA: Springer, 2018, pp. 491–519.

[6] R. Sicari et al., "Stress echocardiography expert consensus statement: European association of echocardiography (EAE)," *Eur. J. Echocardiogr.*, vol. 9, no. 4, pp. 415–437, Jul. 2008.

[7] M. Galderisi, D. Mele, and P. N. Marino, "Quantitation of stress echocardiography by tissue Doppler and strain rate imaging: A dream come true?" *Italian Heart J., Off. J. Italian Fed. Cardiol.*, vol. 6, no. 1, pp. 9–20, 2005.

[8] A. Rösner et al., "Persistent dysfunction of viable myocardium after revascularization in chronic ischaemic heart disease: Implications for dobutamine stress echocardiography with longitudinal systolic strain and strain rate measurements," *Eur. Heart J.-Cardiovascular Imag.*, vol. 13, no. 9, pp. 745–755, Sep. 2012.

[9] L. Hanekom, G.-Y. Cho, R. Leano, L. Jeffriess, and T. H. Marwick, "Comparison of two-dimensional speckle and tissue Doppler strain measurement during dobutamine stress echocardiography: An angiographic correlation," *Eur. Heart J.*, vol. 28, no. 14, pp. 1765–1772, Mar. 2007.

[10] A. C. Ng et al., "Incremental value of 2-dimensional speckle tracking strain imaging to wall motion analysis for detection of coronary artery disease in patients undergoing dobutamine stress echocardiography," *Amer. Heart J.*, vol. 158, no. 5, pp. 836–844, Nov. 2009.

[11] L. T. Yang et al., "Strain imaging with a bull's-eye map for detecting significant coronary stenosis during dobutamine stress echocardiography," *J. Amer. Soc. Echocardiogr.*, vol. 30, no. 2, pp. 159–167. Feb. 2017.

[12] P. Reant et al., "Experimental validation of circumferential, longitudinal, and radial 2-dimensional strain during dobutamine stress echocardiography in ischemic conditions," *J. Amer. Coll. Cardiol.*, vol. 51, no. 2, pp. 149–157, Jan. 2008.

[13] E. A. Bunting, J. Provost, and E. E. Konofagou, "Stochastic precision analysis of 2D cardiac strain estimationin vivo," *Phys. Med. Biol.*, vol. 59, no. 22, pp. 6841–6858, Oct. 2014.

[14] P. L. Castro et al., "Potential pitfalls of strain rate imaging: Angle dependency," *Biomed. Sci. Instrum.*, vol. 36, pp. 197–202, Jan. 2000.

[15] J. Poree, M. Baudet, F. Tournoux, G. Cloutier, and D. Garcia, "A dual tissue-Doppler optical-flow method for speckle tracking echocardiography at high frame rate," *IEEE Trans. Med. Imag.*, vol. 37, no. 9, pp. 2022–2032, Sep. 2018.

[16] C. Ma and T. Varghese, "Comparison of cardiac displacement and strain imaging using ultrasound radiofrequency and envelope signals," *Ultrasonics*, vol. 53, pp. 782–792, Mar. 2013.

[17] J. Grondin, M. Waase, A. Gambhir, E. Bunting, V. Sayseng, and E. E. Konofagou, "Evaluation of coronary artery disease using myocardial elastography with diverging wave imaging: Validation against myocardial perfusion imaging and coronary angiography," *Ultrasound Med. Biol.*, vol. 43, no. 5, pp. 893–902, May 2017.

[18] V. Tavakoli et al., "Tissue Doppler imaging optical flow (TDIOF): A combined B-mode and tissue Doppler approach for cardiac motion estimation in echocardiographic images," *IEEE Trans. Biomed. Eng.*, vol. 61, no. 8, pp. 2264–2277, Aug. 2014.

[19] W. N. Lee and E. E. Konofagou, "Angle-independent and multi-dimensional myocardial elastography—From theory to clinical validation," *Ultrasonics*, vol. 48, nos. 6–7, pp. 563–567, 2008.

[20] S. J. Okrasinski, B. Ramachandran, and E. E. Konofagou, "Assessment of myocardial elastography performance in phantoms under combined physiologic motion configurations with preliminaryin vivofeasibility," *Phys. Med. Biol.*, vol. 57, no. 17, pp. 5633–5650, Aug. 2012.

[21] J. D'hooge et al., "Regional strain and strain rate measurements by cardiac ultrasound: Principles, implementation and limitations," *Eur. J. Echocardiogr.*, vol. 1, no. 3, pp. 154–170, Sep. 2000.

[22] A. Hodzic et al., "Accuracy of speckle tracking in the context of stress echocardiography in short axis view: An in vitro validation study," *PLoS ONE*, vol. 13, no. 3, Mar. 2018, Art. no. e0193805.

[23] T. Varghese, J. Ophir, E. Konofagou, F. Kallel, and R. Righetti, "Tradeoffs in elastographic imaging," *Ultrason. Imag.*, vol. 23, no. 4, pp. 216–248, Oct. 2001.

[24] J. Grondin, V. Sayseng, and E. E. Konofagou, "Cardiac strain imaging with coherent compounding of diverging waves," *IEEE Trans. Ultrason., Ferroelectr., Freq. Control*, vol. 64, no. 8, pp. 1212–1222, Aug. 2017.

[25] A. Rösner, D. Barbosa, E. Aarsæther, D. Kjønås, H. Schirmer, and J. D'hooge, "The influence of frame rate on two-dimensional speckle-tracking strain measurements: A study on silico-simulated models and images recorded in patients," *Eur. Heart J.-Cardiovascular Imag.*, vol. 16, no. 10, pp. 1137–1147, Mar. 2015.

[26] J. Luo and E. E. Konofagou, "High-frame rate, full-view myocardial elastography with automated contour tracking in murine left ventricles in vivo," *IEEE Trans. Ultrason., Ferroelectr., Freq. Control*, vol. 55, no. 1, pp. 240–248, Jan. 2008.

[27] M. Cikes, L. Tong, G. R. Sutherland, and J. D'Hooge, "Ultrafast cardiac ultrasound imaging: Technical principles, applications, and clinical benefits," *JACC Cardiovascular Imag.*, vol. 7, no. 8, pp. 812–823, Aug. 2014.

[28] C. Papadacci, M. Pernot, M. Couade, M. Fink, and M. Tanter, "High-contrast ultrafast imaging of the heart," *IEEE Trans. Ultrason., Ferroelectr., Freq. Control*, vol. 61, no. 2, pp. 288–301, Feb. 2014.

[29] L. C. N. Lervik et al., "Myocardial strain rate by anatomic Doppler spectrum: First clinical experience using retrospective spectral tissue Doppler from ultra-high frame rate imaging," *Ultrasound Med. Biol.*, vol. 43, no. 9, pp. 1919–1929, Sep. 2017.

[30] M. V. Andersen et al., "High-frame-rate deformation imaging in two dimensions using continuous speckle-feature tracking," *Ultrasound Med. Biol.*, vol. 42, no. 11, pp. 2606–2615, Nov. 2016.

[31] L. Tong, A. Ramalli, R. Jasaityte, P. Tortoli, and J. D'hooge, "Multi-transmit beam forming for fast cardiac imaging—Experimental validation and in vivo application," *IEEE Trans. Med. Imag.*, vol. 33, no. 6, pp. 1205–1219, Jun. 2014.

[32] L. Tong et al., "Wide-angle tissue Doppler imaging at high frame rate using multi-line transmit beamforming: An experimental validation in vivo," *IEEE Trans. Med. Imag.*, vol. 35, no. 2, pp. 521–528, Sep. 2016.

[33] S. Wang, W.-N. Lee, J. Provost, J. Luo, and E. E. Konofagou, "A composite high-frame-rate system for clinical cardiovascular imaging," *IEEE Trans. Ultrason., Ferroelectr., Freq. Control*, vol. 55, no. 10, pp. 2221–2233, Oct. 2008.

[34] G. Montaldo, M. Tanter, J. Bercoff, N. Benech, and M. Fink, "Coherent plane-wave compounding for very high frame rate ultrasonography and transient elastography," *IEEE Trans. Ultrason., Ferroelectr., Freq. Control*, vol. 56, no. 3, pp. 489–506, Mar. 2009.

[35] D. Wang et al., "Ultrafast myocardial elastography using coherent compounding of diverging waves during simulated stress tests: An in vitro study," in *Proc. IEEE Int. Ultrason. Symp.*, Sep. 2017, pp. 1–4.

[36] J. Poree et al., "High-frame-rate echocardiography using coherent compounding with doppler-based motion-compensation," *IEEE Trans. Med. Imag.*, vol. 35, no. 7, pp. 57–1647, Jul. 2016.

[37] D. Fleet and Y. Weiss, "Optical flow estimation," in *Handbook of Mathematical Models in Computer Vision*. Boston, MA, USA: Springer, 2006, pp. 237–257.

[38] H. Li, J. Porée, M.-H. Roy Cardinal, and G. Cloutier, "Two-dimensional affine model-based estimators for principal strain vascular ultrasound elastography with compound plane wave and transverse oscillation beamforming," *Ultrasonics*, vol. 91, pp. 77–91, Jan. 2019.

[39] J. Poree et al., "Noninvasive vascular elastography with plane strain incompressibility assumption using ultrafast coherent compound plane wave imaging," *IEEE Trans. Med. Imag.*, vol. 34, no. 12, pp. 31–2618, Dec. 2015.

[40] H. A. Omar, J. S. Domingos, A. Patra, R. Upton, P. Leeson, and J. A. Noble, "Quantification of cardiac bull's-eye map based on principal strain analysis for myocardial wall motion assessment in stress echocardiography," in *Proc. IEEE 15th Int. Symp. Biomed. Imag. (ISBI)*, Apr. 2018, pp. 1195–1198.

[41] R. Nayak et al., "Principal strain vascular elastography: Simulation and preliminary clinical evaluation," *Ultrasound Med. Biol.*, vol. 43, no. 3, pp. 682–699, Mar. 2017.

[42] F. Destrempes, J. Meunier, M.-F. Giroux, G. Soulez, and G. Cloutier, "Segmentation of plaques in sequences of ultrasonic B-mode images of carotid arteries based on motion estimation and a Bayesian model," *IEEE Trans. Biomed. Eng.*, vol. 58, no. 8, pp. 2202–2211, Mar. 2011.

[43] R. Nayak et al., "Principal strain vascular elastography using compounded plane wave imaging," in *Proc. IEEE Int. Ultrason. Symp.*, 2016, pp. 1–4.

[44] G. T. Haar, *The Safe Use of Ultrasound in Medical Diagnosis*. London, U.K.: The British Institute of Radiology, 2012.

[45] F. Tournoux et al., "Estimation of radial strain and rotation using a new algorithm based on speckle tracking," *J. Amer. Soc. Echocardiogr.*, vol. 21, no. 10, pp. 1168–1174, Oct. 2008.

[46] J. Fromageau, J.-L. Gennisson, C. Schmitt, R. L. Maurice, R. Mongrain, and G. Cloutier, "Estimation of polyvinyl alcohol cryogel mechanical properties with four ultrasound elastography methods and comparison with gold standard testings," *IEEE Trans. Ultrason., Ferroelectr., Freq. Control*, vol. 54, no. 3, pp. 498–509, Mar. 2007.

[47] *ACSM's Guidelines for Exercise Testing and Prescription*, A. C. o. S. Med., Lippincott Williams & Wilkins, Baltimore, MD, USA, 2013.

[48] P. S. Douglas et al., "Appropriateness criteria for stress echocardiography: A report of the American college of cardiology foundation appropriateness criteria task force, American society of echocardiography, American college of emergency physicians, American heart association, American society of nuclear cardiology, society for cardiovascular angiography and interventions, society of cardiovascular computed tomography, and society for cardiovascular magnetic resonance endorsed by the heart rhythm society and the society of critical care medicine," *J. Amer. Coll. Cardiol.*, vol. 51, no. 11, pp. 1127–1147, Jan. 2008.

[49] T. Zakaria, Z. Qin, and R. L. Maurice, "Optical-flow-based B-mode elastography: Application in the hypertensive rat carotid," *IEEE Trans. Med. Imag.*, vol. 29, no. 2, pp. 570–578, Feb. 2010.